Attenuation Capacity of a Multi-Cylindrical Floating Breakwater

Martinelli, Luca; Mohamad, Omar; Volpato, Matteo; Eskilsson, Claes; Aufiero, Manuele

Published in:
Journal of Marine Science and Engineering

DOI (link to publication from Publisher):
10.3390/jmse12091550

Publication date:
2024

Document Version
Publisher's PDF, also known as Version of record

Journal of
Marine Science and Engineering

MDPI

Article

Attenuation Capacity of a Multi-Cylindrical Floating Breakwater

Luca Martinelli [1,*], Omar Mohamad [1], Matteo Volpato [1], Claes Eskilsson [2] and Manuele Aufiero [3]

[1] Department of Civil, Environmental and Architectural Engineering (ICEA), Università di Padova, v. Ognissanti, 39, 35129 Padova, Italy; omar.mohamad@studenti.unipd.it (O.M.); matteo.volpato@unipd.it (M.V.)
[2] Department of the Built Environment (BUILD), Aalborg University, Thomas Mann Vej 23, DK-9220 Aalborg, Denmark; claese@build.aau.dk
[3] Sizable Energy S.r.l., Via Giovanni Durando, 39, 20158 Milano, Italy; manuele@sizable-energy.com
* Correspondence: luca.martinelli@unipd.it

Abstract: Floating breakwaters (FBs) are frequently used to protect marinas, fisheries, or other bodies of water subject to wave attacks of moderate intensity. New forms of FBs are frequently introduced and investigated in the literature as a consequence of technological advancements. In particular, a new possibility is offered by High-Density Polyethylene (HDPE) by extruding pipes of large diameters (e.g., 2.5 m in diameter) and with virtually no limit in length (hundreds of meters). By connecting two or three such pipes in a vertical layout, a novel low-cost floating breakwater with deep draft is devised. This note investigates numerically and experimentally the efficiency of this type of multi-cylindrical FBs in evaluating different geometries and aims at finding design guidelines. Due to the extraordinary length of the breakwater, the investigation is carried out in two dimensions. The 2D numerical model is based on the solution of the rigid body motion in the frequency domain, where the hydrodynamic forces are evaluated (thanks to a linear potential flow model), and the mooring forces do not include dynamic effects nor drag on the lines. The numerical predictions are compared to the results of a 1:10 scale experimental investigation. An atypical shape of the wave transmission (k_t) curve is found, with a very low minimum in correspondence with the heave resonance frequency. The results essentially point out the influence of the position of the gravity center, the stiffness, and the mutual distance among cylinders on k_t.

Keywords: floating breakwaters; cylinders; experimental modeling; numerical modeling; transmission coefficient

Citation: Martinelli, L.; Mohamad, O.; Volpato, M.; Eskilsson, C.; Aufiero, M. Attenuation Capacity of a Multi-Cylindrical Floating Breakwater. *J. Mar. Sci. Eng.* **2024**, *12*, 1550. https://doi.org/10.3390/jmse12091550

Academic Editor: Constantine Michailides

Received: 12 July 2024
Revised: 28 August 2024
Accepted: 1 September 2024
Published: 4 September 2024

1. Introduction

The first relevant applications of floating breakwaters (FBs) were the Phoenix and the Bombardon FBs, constructed by the British Corps of Engineers and the British Navy during World War II, and crucial for Normandy landings operations [1]. Since then, different types of FBs have been used to protect marinas, fisheries, or other bodies of water subject to wave attacks of moderate intensity. FBs are an economical and environmentally friendly option, especially in deeper waters (e.g., 10 m), where the cost of the foundation may be very competitive compared to other solutions, or when the tidal range is relevant (e.g., >0.5 m) since in order to have an effective defense, the structure freeboard is necessarily high, thus creating a large visual impact in low-tide conditions. The main disadvantage is that the reflection and transmission coefficients are frequency dependent, and especially long waves are poorly attenuated [2,3].

There exist several types of FBs [4,5]. Some examples are the box type, one of its variants, the Π type (with lateral wings), and the framed FBs; see Figure 1.

Box-type FBs are basically rigid massive structures with a simple geometry, and wave attenuation is achieved mainly by reflection. The attenuation capacity of a box-type FB is well defined, for instance, by the classical Macagno formula [6], that states that the

transmission coefficient k_t (defined as the ratio of transmitted wave height over the incident wave height) may be written as

$$k_t = \frac{1}{\sqrt{1 + \left(\frac{kB\sinh(k_i h)}{2\cosh(kh - kd)}\right)}} \quad (1)$$

in which k is the wave number, h is the still water depth, and B and d are, respectively, the width and draft of FB. The Macagno formula is based on linear potential flow (LPF) theory for a fixed box in constant depth, and we may observe that it depends on two non-dimensional variables, i.e., the relative draft kd and the relative width kw.

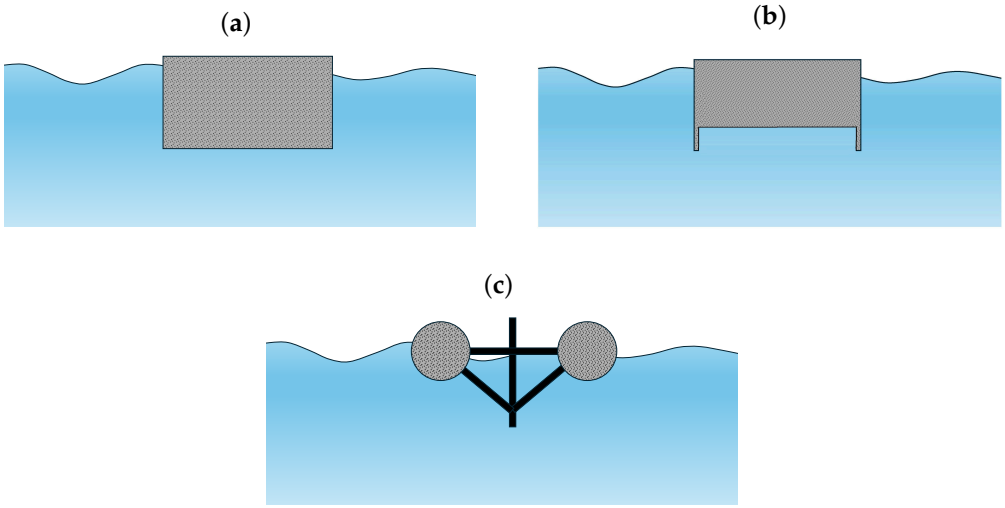

Figure 1. Floating breakwaters: (**a**) box-type, (**b**) pontoon-type, and (**c**) framed-type.

Early experimental studies of box-shaped FBs investigated different geometries in order to find a more cost-effective solution [7–9]. They concluded that an effective box-type FB should have sufficient draft under the water surface and should have a comparatively large displaced water volume. In other terms, in order to attenuate the incident waves, the natural oscillation period of the floating body must be large enough as compared with that of the incident wave [7].

The Π-type design (Figure 1b) takes advantage of this concept. It has the same working principle as the box-type but exhibits enhanced performance since it has a larger inertia (the water trapped by the lateral wings increases the added mass). The study on Π-type FBs [10] proposed a modification to the Macagno formula to account for typical moorings (i.e., not-fixed FBs). The modified formula is rewritten in terms of a single non-dimensional variable (rather than two) representing the ratio between the wave period and the natural heave period (T_n) for an unconstrained structure. T_n is defined for box-type FBs regardless of the type of constraint as

$$T_n = 2\pi\sqrt{\frac{d + 0.35w}{g}} \quad (2)$$

where d is the draft, w is the beam width, and g is the acceleration of gravity. Since the ratio T_p/T_n effectively replaces both the non-dimensional wavelength and the non-dimensional draft as also confirmed by [11] for porous structures, it is a more convenient variable against which to plot the transmission coefficient. In general, box-type FBs are not efficient when the peak period of incident waves is significantly larger than T_n.

Frame-type FBs (Figure 1c) are frequently composed of small cylinders (pipes) and attenuate the waves mainly by reflection and turbulent losses caused by the frames. Recently, a novel multi-cylindrical FB design was suggested that is based on large cylindrical pipes that are vertically aligned. The design is a result of technological advancements in low-cost Extruded High-Density Polyethylene (HDPE) pipes with large diameters (e.g., 2.5 m) and

thicknesses of 5 to 10 cm. These pipes can be extruded directly at sea, reaching virtually unlimited lengths of hundreds of meters [12]. By vertically connecting two or three of these piles through heavy concrete clamps, a low-cost FB can be constructed. The lower fully submerged pipes are filled with water, while the upper pipe is empty and provides enough buoyancy to maintain a freeboard of half the diameter for the entire combination. This large multi-cylindrical FB, which is allowed to heave and roll, has a large mass and hence its performance could be, in part, similar to that of a box-type FB, but some differences are expected due to the low center of gravity.

This paper will present, to the author's best knowledge, the first investigation on wave transmission past a vertically aligned multi-cylindrical FB. The aim of this note is to study the efficiency of this type of structure and offer some preliminary design guidelines. The performance of the multi-cylindrical FB will be examined in terms of transmission coefficients (k_t) and Response Amplitude Operators (RAOs). Several different configurations are tested, both experimentally and numerically, and the effects of the location of the center of gravity (CG) and mooring stiffness are examined. The investigation is performed in two dimensions to conveniently represent the extraordinary length of the breakwater.

The paper is organized as follows. A short literature review is presented in Section 2, focusing on existing studies on loads and motions of horizontal cylinders, especially studies looking into setups of two or three cylinders. Section 3 describes the experimental methodology used to analyze the performance of the multi-cylindrical FB. It is divided in two subsections: First, the tests are described in detail. Then, the results are shown, pointing out the peculiar attenuation trend and the necessity for an interpretative framework. Section 4 describes the application of a simple numerical model used to interpret the experimental results (the model implementation is presented in Appendix A). In Section 5, the numerical model is used to check if it is possible to reproduce the observed experimental trend in terms of Response Amplitude Operators (RAOs) and transmission coefficients and to investigate the influence of the depth of CG, the overall inertia, and the stiffness of the mooring lines on the FB performance. Finally, in Section 6, the study is summarized, and the conclusions and some design guidelines are presented.

2. Cylindrical FBs

This section recalls a number of investigations that are particularly relevant for the type of floating breakwater here analyzed, i.e., based on a combination of cylinders. In particular, the focus is placed on two-dimensional studies, i.e., those representing the behavior of a very long structure such as a breakwater.

Single partially submerged cylinders have long been studied due to their relevance to ship design. For instance, Ursell [13] shows the expressions of the added mass and the scattered wave due to small heaving oscillations of a horizontal cylinder in 2D, followed by experimental [14] investigations. The 2D motion of a partially submerged cylinder is also presented in [15]. Borgman [16] studies the effect of oblique waves. Frank in [17] presents a computer program for calculating the hydrodynamic pressure, force, and moment of fluids on cylinders, using the 2D Green function. The approach cannot be directly applied to the structure investigated in this paper due to the presence of a lower cylinder, but it basically proves that the theoretical background for a numerical investigation was already present. In [18], the complete expressions of added mass and damping for heave, sway, and roll motion with coupling coefficients for sway and roll are given. The theoretical solution of the hydrodynamics of a half-immersed cylinder in infinite water depth, studied in two dimensions under beam seas (i.e., with the structure's longitudinal axis parallel to the incident wave crests) is studied in [19]. With regard to the resonance period of a cylinder, [10] shows that the theoretical value of the added mass of a cylinder is $0.39D$, where D is the diameter. Assuming that the FB is cylindrical and semi-submerged and that the added mass is negligible, the reference period may therefore be assumed to be $T_n \approx 2\pi\sqrt{0.4D/g}$.

When a floating structure is composed of two rigidly connected identical cylinders, the most commonly studied shape is the horizontal alignment. It is studied, for instance, in [20], where the free surface potential problem is solved, and in [21,22], where a CFD model is used for the numerical modeling, coupled for the free surface to a level-set method and a volume of fluid method, respectively. In [23], a smooth particle hydrodynamic model is used, and since the pair of cylinders is actually interpreted as a floating breakwater, the transmission coefficients are also given. For this type of structure, the experimental transmission coefficient curve is given by [11].

Conversely, the combination of two or more cylinders vertically aligned has not particularly been investigated. To our knowledge, it is only studied in [24], where the hydrodynamics for the case of two fixed semi-submerged cylinders with different vertical spacing between them is numerically simulated. The cylinder sizes are based on the single cylinder study of [25]. The paper shows the wave loads on the cylinders, the wave run-up, and the overtopping, and does not discuss the transmission coefficient since the device is not specifically intended as a floating breakwater. Other studies involve structures combining three cylinders, aligned either horizontally or in a triangular shape (i.e., two cylinders that are surface-piercing and one that is fully submerged). In [26], the attenuation performance of the FB formed by three cylinders is compared to the single-cylinder behavior, under different mooring types. A disposition where the three pipes are more distant, in a frame, is studied in [27]. These breakwaters may be considered to be of the frame type. In [28], the theoretical background for combining many (albeit non-vertically overlapping) bodies is presented, with an application to an array of 33 (3 × 11) vertical cylindrical legs.

In conclusion, we did not find in the literature the transmission coefficient curve specific for a floating breakwater composed by two or three vertically aligned cylinders.

3. Physical Modeling

3.1. Test Description

An experimental investigation on vertically aligned multi-cylindrical FBs at a Froude scale of 1:10 has been carried out in the wave flume at the Maritime Laboratory, ICEA Department, University of Padova. The flume is 36.0 m long, 1.0 m wide, and has a water depth at the structure of $h = 0.875$ m. The wavemaker is of the piston type with active absorption. On the side of the channel opposite the wavemaker, there is a sloping gravel beach and a floating heavy porous mattress (made of foam) to minimize wave reflection.

Three different FB configurations are tested (see Figure 2 and Table 1). Configuration A consists of two pipes, each with a 250 mm diameter, spaced 400 mm apart. Configuration B replicates A but includes an additional 125 mm diameter pipe positioned between the larger pipes. Configuration C comprises two pipes with a 250 mm diameter and a mutual distance of 300 mm. In each FB configuration, the two or three pipes are rigidly connected to form a single rigid body. All pipes are 0.98 m long, to fit the channel width. The top tube is sealed at both ends to prevent the passage of water, while the other tube(s) remain open to allow water inside the tube. In practice, these massive elements have a marginal submerged weight. An external steel frame assures that the structures behave as a single rigid body and prevents the structure itself from breaking. Symmetrically arranged steel rods weighing a total of 13.6 kg are inserted into the lower cylinder. These rods provide the necessary counterweight and, at the same time, improve the stability of the model.

Table 1. Dimensions of the drawing with 3 configurations.

Configurations	D_1 (mm)	D_2 (mm)	d (mm)	h (mm)	K (N/m)
Config. A	250	None	400	875	1200
Config. B	250	125	400	875	1200
Config. C	250	none	300	875	1200

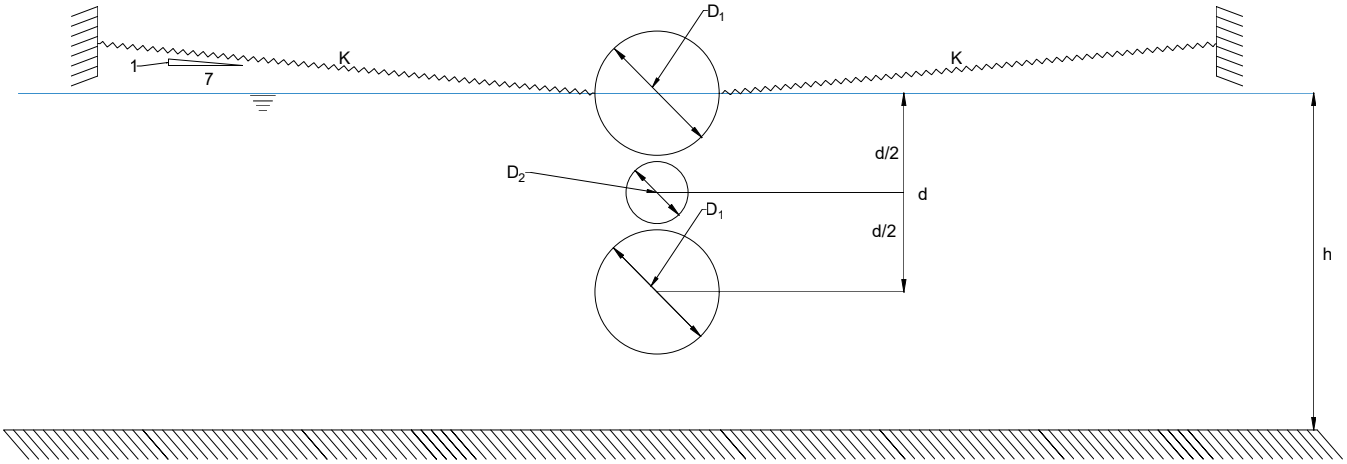

Figure 2. Experimental setup. Cross view of the tested FB models with 2 or 3 pipes.

The FB is moored by four lines (Figure 3), each equipped with a strain gauge to measure the axial load. The lines are non-stretchable (Kevlar fibers) suspended by steel springs that simulate the elasticity of the prototypical compliant mooring. The lines are pre-stressed to avoid slack conditions; therefore, the four lines are always in tension, and the global stiffness is four times the stiffness of the single line. In order to provide enough flexibility and elongation to allow the spring to stretch within the elastic range, each anchoring line is tied by nine springs arranged in three parallel groups. The global mooring system yields a reaction force of approximately 1000 N/m and an elongation larger than 0.6 m.

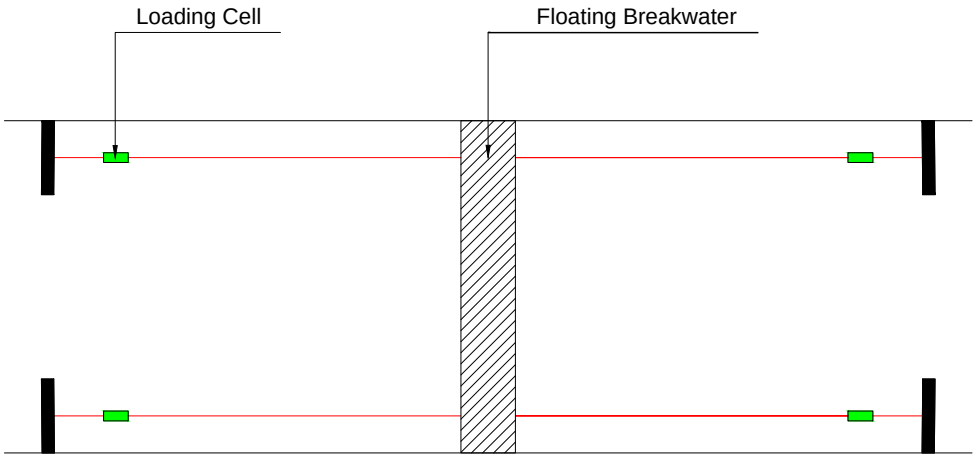

Figure 3. Top view: mooring lines and load cells.

Some of the tests for Configuration A are repeated two times, changing the pre-stress levels F_o from 25 N to 70 N. Only the latter pretension assures that the line never gets slack during all wave conditions and is therefore used for all the tests in Configurations B and C.

Figure 4 provides an image of the breakwater of Configuration A under the wave action.

All data recordings are triggered by the same command, thereby enabling the implementation of smart, efficient, and integrated monitoring and analysis. The measured quantities are as follows:

- The incident, reflected, and transmitted waves through two arrays of four resistive wave gauges (WGs) placed in front of (offshore) and behind (shoreward) the FB, logged at 100 Hz;

- The load along the four mooring lines, through four full bridge load cells with maximum load 250 N, analog lowpass-filtered at 500 Hz and subsequently logged at 1200 Hz;
- The movements in sway, heave, and roll, captured by a two-megapixel webcam placed in front of the glass, recorded at 60 fps.

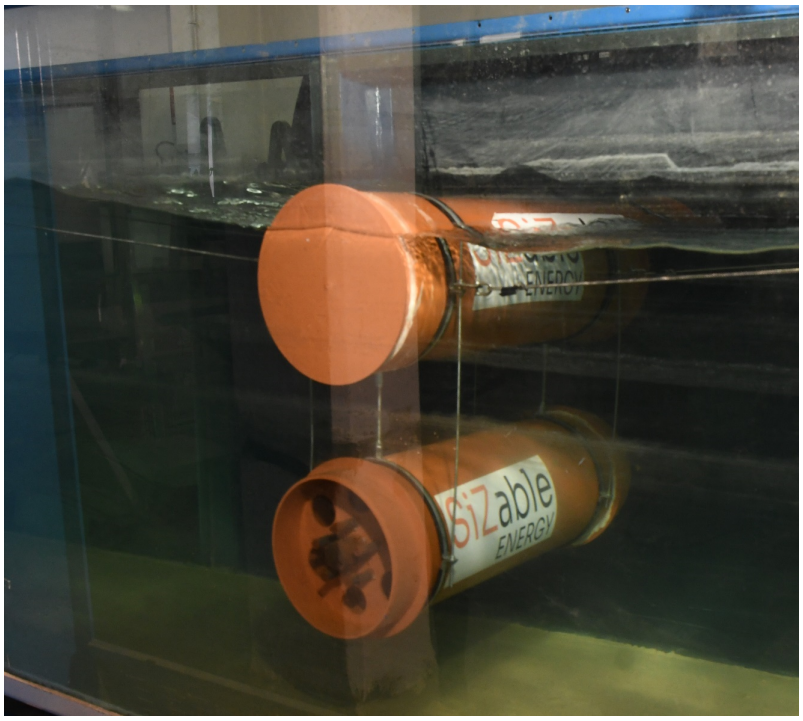

Figure 4. Tested FB (Config. A).

In order to better approximate the real behavior of the structure, the experimental study considered both regular and irregular wave conditions. Nevertheless, waves in the flume are necessarily perpendicular and long-crested, whereas in reality, the wave hits the structure with an obliquity ranging from 0° to 90° and, in general, a non-null directional dispersion. We expect, as shown for box-type FB in [29] through an eigenfunction expansion method, that the transmission is lower with increased obliquity for all waves. For a perpendicular wave attack, the directional dispersion is then also expected to reduce the transmission coefficient. This behavior does not seem to be generalized, however. Gesraha [30], based on the same eigenfunction technique, finds that a freely floating pi-type breakwater is more protected from waves in the case of normally incident short waves (i.e., shows a lower kt for perpendicular waves in case they have high frequency). For moored pi-type FBs, in [31], it is experimentally found that there is a significant reduction in kt for oblique waves. Ji et al. [11] for a cylindrical (horizontally placed) pair of cylinders, find that the transmission coefficient at 0° and 30° obliquity is similar.

The test program is given graphically in Figure 5 and includes regular and irregular waves. The blue stars show the target incident wave characteristics generated for all configurations, with a spring pretension of 70 N. The tests carried out also for a lower pretension (25 N), only for Configuration A, are indicated by a red circle. Regular waves have a (target) wave period T varying between 0.5 s and 1.6 s and a (target) wave height H varying between 0.01 and 0.16 m (upper panel in Figure 5). Irregular waves have a (target) peak period T_p also in the range 0.5 s–1.6 s, whereas irregular waves have a (target) significant wave height H_s varying between 0.02 m and 0.14 m (lower panel in Figure 5). The tests used in the following sections for evaluating the Response Amplitude Operators (RAOs) and the transmission coefficient are only those connected by a blue line.

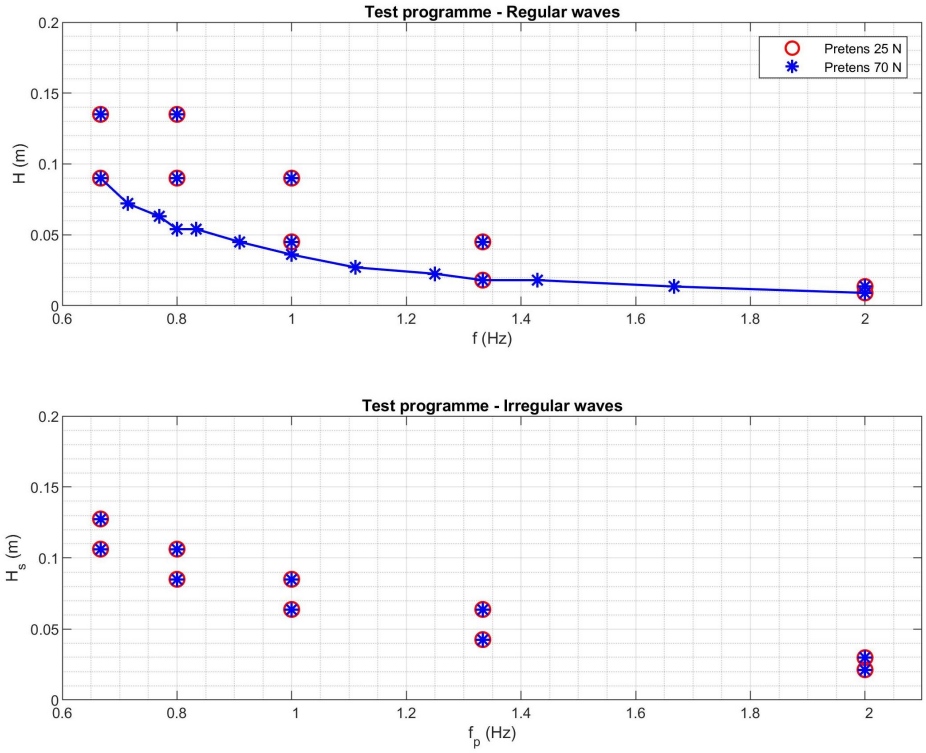

Figure 5. Test program (Config. A). The measured incident wave conditions are given in graphical form.

3.2. Results in Terms of Wave Transmission

The FB performance is the measure of its attenuation capacity, described through the wave transmission coefficient k_t, i.e., the ratio between the transmitted (H_t) and incident (H_i) wave heights. The incident and reflected waves are identified and separated following the procedure proposed by [32]. In order to calculate the experimental k_t, it is therefore necessary to find the incident and reflected wave heights. These values are not completely constant even during regular wave conditions. Hence, the regular wave tests are processed as follows: a specific time window of 60 s is selected, in the middle of the test, checking that stationary conditions are reached. The incident and reflected components measured at the two arrays of wave gauges, one placed in front and one behind the FB, are separated, to find the incident and transmitted wave components. The regular wave height is almost constant, and the considered value is actually the rms characteristic wave height value:

$$k_t = \frac{H_t}{H_i} \tag{3}$$

Figure 6 shows the experimental k_t for all configurations as a function of the frequency of the incident waves. The curve is very different from the typical S-shape trend. Even if the frequency step is small, there is no evident trend. Of course, the response at high frequency (close to 2 Hz) is not particularly relevant, and the waves generated in the lab are a bit distorted since the wavemaker has a low-pass filter to avoid transversal waves.

For irregular waves, the height is defined in a similar procedure as for the regular wave tests, except that the duration of the analyzed time windows is 30 min. The wave transmission coefficient is plotted in Figure 7 as a function of the measured peak wave frequency, which is slightly different from the target one.

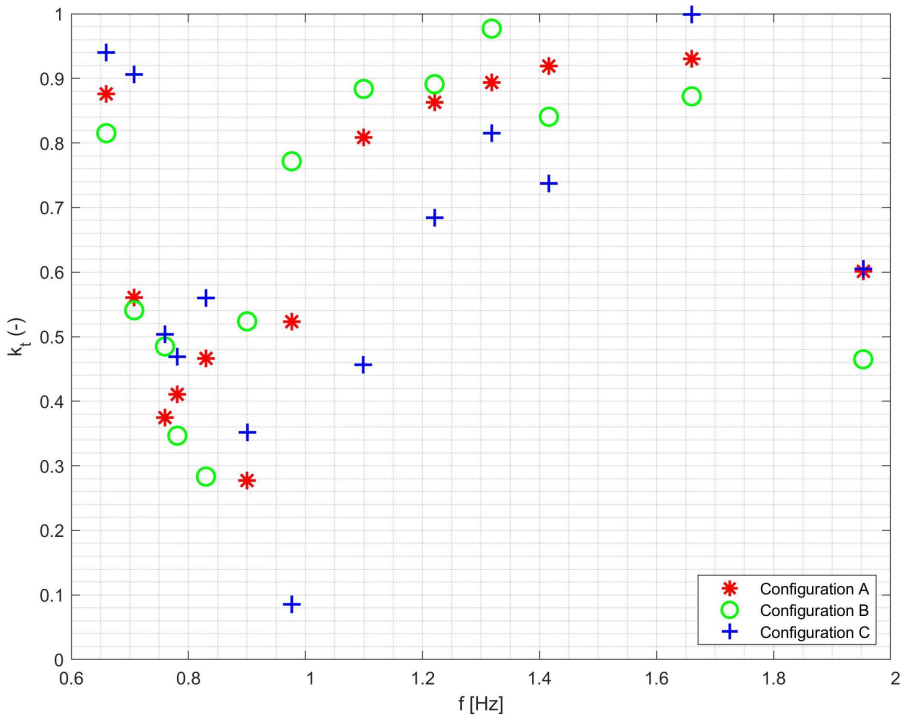

Figure 6. Transmission coefficient (regular waves). It is difficult to understand the trend in the absence of an interpretative model.

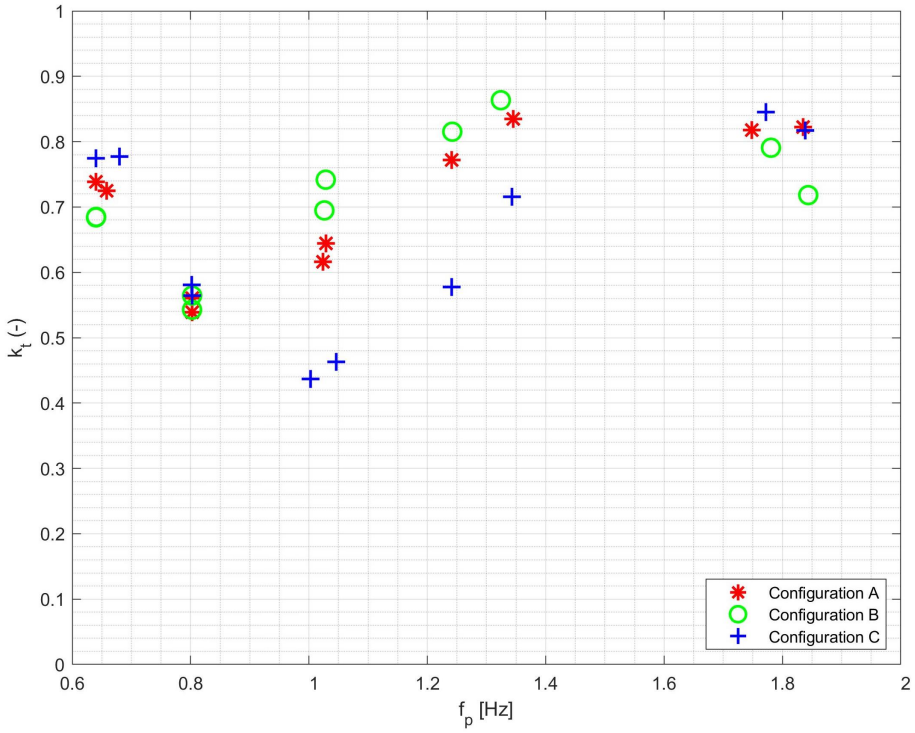

Figure 7. Transmission coefficient (irregular waves).

The trend of the k_t curve presented in Figures 6 and 7 is puzzling. It is rather different from the typical curve that characterizes box-type FB, where the transmission decreases with frequency. On the contrary, we see that for a wide range of frequencies, the transmission increases. The plots reflect the observed behavior. For some low frequencies, the FB fully

reflects the incident wave. For other larger frequencies, the FB rotates around a low center and irradiates a wave that is almost equal to the incident one.

In order to better understand the process and support the data reliability, it is necessary to build a model of the expected behavior. Hence, in the next section, a simple numerical model is presented.

4. Numerical Model

A simple numerical model based on linear potential flow (LPF) theory [33] is implemented in order to understand if the experimental behavior (described in Section 3) may be considered acceptable. LPF is based on the assumptions that the fluid is inviscid and incompressible, and the flow is irrotational, as well as that the wave and motion amplitudes are small.

Details of the model are given in Appendix A.

In [34], the movements of a floating sphere are measured and compared with the results of different types of numerical models, showing that the simple linear potential flow model accuracy is acceptable even for very large displacements. Hence, this simplified approach is considered sufficiently accurate for the aims of this paper.

Data Used in the Numerical Model

The reference system used for the description of the movements has a vertical z-axis, a horizontal x-axis aligned with the wave propagation direction, and a center corresponding to the center of the upper pipe (at rest condition), and the rotations are positive in the clockwise direction. As a consequence, the stiffness matrix is diagonal but the mass matrix is not because a rotation induces a movement of the CG. The global horizontal stiffness C_x is given by the four springs, which partly contributes also to the vertical stiffness (due to the slope of the lines, $\tan(\alpha)$ = 1:7). The measured stiffness of each spring at rest is 260 N/m so that the four springs give a total of 1040 N/m. A small calibration procedure is used to fit the model predictions to the data achieved from Configuration A. Then, a coherent method across the three models is followed. According to this procedure, in order to better fit the curve measured for the sway oscillations in Configuration A, a larger horizontal stiffness is assumed, i.e., 30% larger ($C_x = 1350$ N/m). This may be due to the non-linear behavior of the springs, whose stiffness is linearized around the initial condition (pretension of approximately 70 N).

The vertical hydrodynamic stiffness is proportional to the wet area. If the FB is in undeformed (undisturbed) conditions, the wet area is given by DL_p, where D is the upper pipe diameter (0.250 m) and L_p is the pipe length (1.0 m). This is rarely the real wet area though since the pipe is either higher or lower than the initial still condition, and in both cases, the vertical hydrodynamic stiffness is lower. A better fit to the experiments is achieved by linearizing the vertical stiffness close to the operating conditions, hence considering a wet area equal to 90% of the undisturbed one. Therefore, the vertical stiffness (sum of the hydrodynamic and the mooring components) is given by $C_z = 0.9\rho g D L_p + C_x \tan(\alpha)$.

The rotational stiffness is simply $C_\phi = \rho g V (d_M - d_g)$, where V is the submerged volume, d_g is the gravity center, and d_M is the metacenter.

The mass matrix is characterized by a single non-diagonal term arising from the coupling between roll and sway, and it is the mass multiplied by d_g. Mass M, inertia $I_{\phi\phi}$ around the axis of the upper pipe, V, d_g and d_M are given in Table 2 for the tested configurations. It may be noted that there is a small deviation between the buoyancy and weight due to the vertical contribution of the mooring pretension.

Finally, in order to achieve a better match between simulations and measurements, a small damping in the vertical direction is also assumed: $B_z = 0.07\rho H A_v$, where H is the wave height and A_v is the sum of the vertical footprint of the pipes, i.e., $\sum A_v = D_i L_p$, where D_i is the pipe diameters and i spans from 1 to 2 (Configurations A and C) or to 3 (Configuration B).

Table 2. Characteristics of the 3 configurations.

Configurations	A	B	C
Mass (kg)	77.7	87.2	77.7
Inertia (kg·m^2)	13.15	13.44	6.95
Volume (m^3)	0.0736	0.0831	0.0736
d_G (m)	0.380	0.370	0.285
d_M (m)	0.266	0.256	0.200

5. Numerical Interpretation

In this section, the model is applied with the settings described above and compared to the experimental results. Regular wave tests are generated. The purpose is to check if there are large deviations (visually detectable) and hence the possible presence of gross errors in the observed experimental trend. Then, the model is also applied to predict the effect of major design variables. In fact, it is interesting from a design point of view to investigate how the FB performance depends on parameters that do not significantly affect the total cost, such as the radius of gyration, mutual distance between the piles, and stiffness. The developed numerical model is used to vary these parameters, using Configuration A as a baseline under regular waves. Even if the accuracy of the model results is not fully demonstrated, the analysis is useful to point out how the structure behavior depends on these factors.

5.1. Measured Oscillations

The footage of the webcam, showing the pipe position through the glass wall from a perpendicular point of view, is analyzed using the Matlab image processing toolbox [35]. In each frame of the video, the circular shape and the central position of the pipes are automatically detected, without the need for specific markings. There is no need for calibration since the diameter of the pipes is measured in pixels and associated with the known pipe diameter. This allows for tying screen movements in pixels to physical model measurements, yielding time series data for the floating body oscillations related to the horizontal, vertical, and roll movements.

The RAOs (Response Amplitude Operators) for heave and sway are defined by

$$RAO_{SWAY} = \frac{A_{SWAY}}{H/2} \tag{4}$$

where A_{SWAY} is the average horizontal oscillation amplitude of the midpoint of the upper cylinder, and H is the regular incident wave height:

$$RAO_{HEAVE} = \frac{A_{HEAVE}}{H/2} \tag{5}$$

where A_{HEAVE} is the average vertical oscillation amplitude of the midpoint of the upper cylinder:

$$RAO_{ROLL} = \frac{A_{ROLL}}{H/(2L)} \tag{6}$$

where A_{ROLL} is the average horizontal rotation in radians, and L is the regular incident wavelength.

Figures 8–10 show the experimental values of the RAOs for sway, heave, and roll as a function of the frequency of the incident wave. The numerical prediction is also added to the figures. The incident wave height varies with the frequency and is given in Figure 5. In short, it can be noticed that the experimental results are pretty regular and aligned, except for the roll RAOs for Configuration B at low frequency. The agreement between experiments and prediction is not perfect, but the model is sufficiently accurate to predict the trend in many cases.

A more detailed description of the RAO graphs is given below. The experimental RAOs for heave are presented in Figure 8. Heave is independent of the other oscillation modes, and, in fact, the results show a typical resonator response. A clear peak is detectable for Configurations A and C (which the model can reproduce thanks to the assumption on the vertical stiffness described above), whereas the peak value of the curve for Configuration B is not obvious. In the range between 0.75 Hz and 0.85 Hz, the measured values for Configurations A and B show a small irregular step, not interpreted by the numerical model. At 1.2 Hz, the experimental measurement for Configuration B is slightly larger than a regular pattern would suggest.

Given the inviscid hypotheses, it is expected that the model will predict larger oscillations than the experiments. This is not true for the heave (where the damping coefficient B_z is used to achieve the observed value fitting). For the other oscillation modes, the only damping is the hydrodynamic one (B matrix in Equations (A8) and (A9)).

The model predictions are in reasonably good agreement with the data, showing a smaller error for Configuration A than for the other models. Actually, the calibration procedure is limited since the weight is known, and the stiffness is calibrated as explained above (to fit Configuration A). The aforementioned irregularities in the dataset are larger than the average distance between predictions and measurements, and therefore we consider the comparison satisfactory.

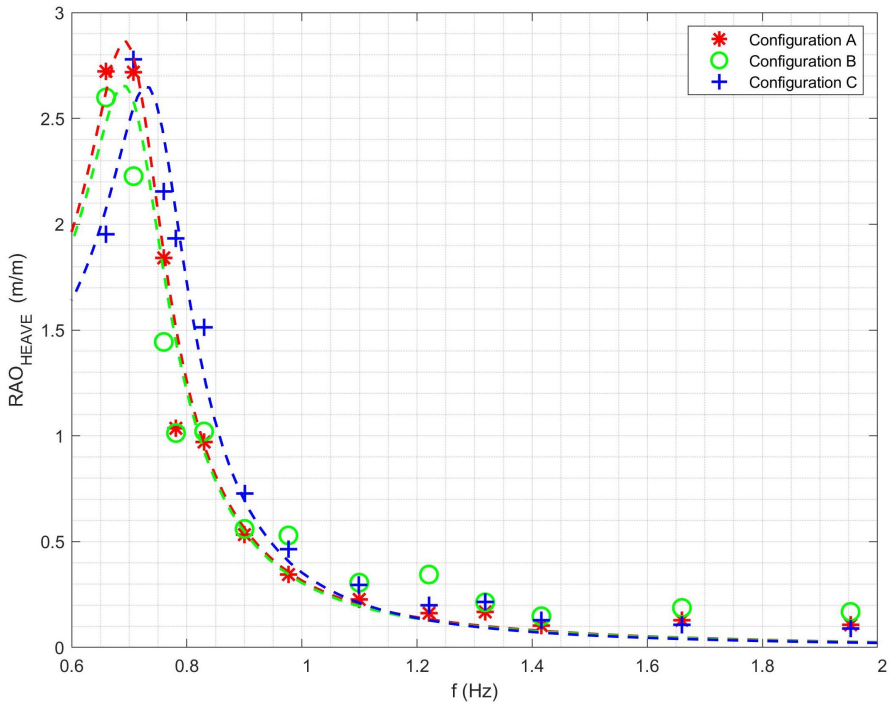

Figure 8. Experimental values (markers) and numerical predictions (dashed lines) of RAO_{HEAVE}.

The experimental RAOs for sway (Figure 9) and roll (Figure 10) interpret a rigid body motion that is the sum of two rotations around a low and a high center.

For the sway, the trend in the measurement is regular in general, with the exception of a few points. The observed trend and the differences among the different configurations are correctly predicted by the model in the whole range of frequencies. In particular, all RAOs for Configuration A are larger than those for Configuration C. For frequencies $f \geq 1.15$ Hz, the RAOs for Configuration C become larger than those for Configuration B. For $f \geq 0.95$ Hz, the RAOs for Configuration A become larger than those for Configuration B. Quantitatively, there are some differences. The data uncertainty does not allow us to pinpoint the exact RAO peak position; nevertheless, the experimental trend regularity is sufficient to suggest that the predicted peak positions have an error lower than 0.1 Hz.

For Configuration C, the model overpredicts the horizontal RAO in the frequency range between 0.75 Hz and 1.0 Hz.

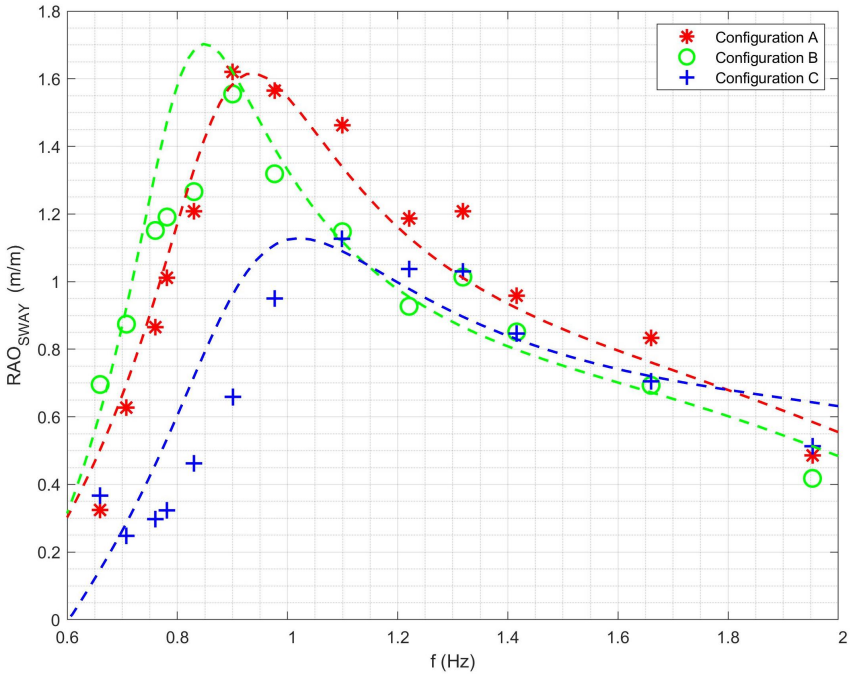

Figure 9. Experimental values (markers) and numerical predictions (dashed lines) of RAO_{SWAY}.

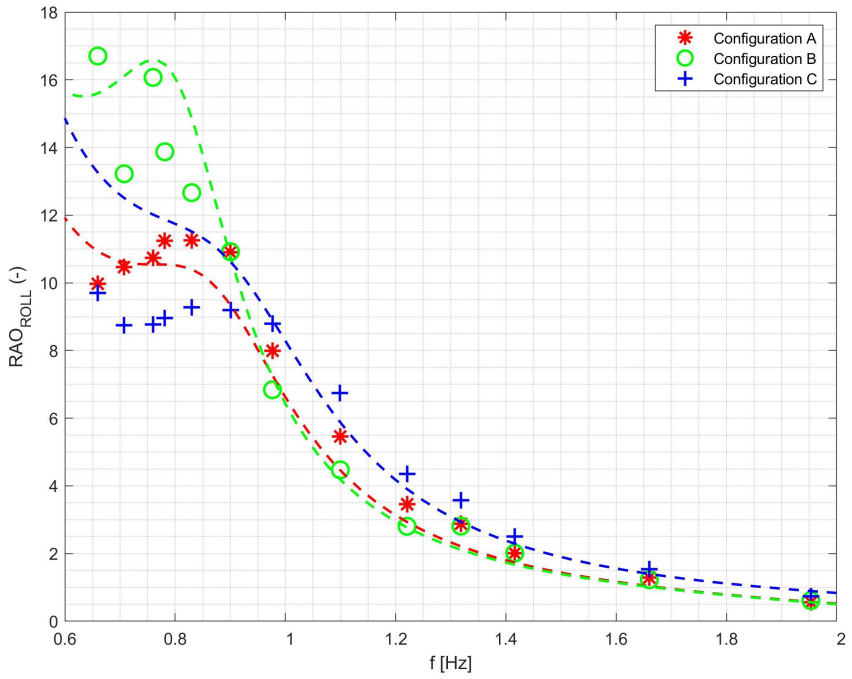

Figure 10. Experimental values (markers) and numerical predictions (dashed lines) of RAO_{ROLL}.

The observed RAOs for and roll are regular (follow a smooth curve), except for Configuration B, for $f \leq 1.15$ Hz, where points irregularly oscillate between 13.5 and 16. In the same frequency range, the predicted RAOs for roll relative to Configuration C deviate significantly from the observations (for instance, at $f = 0.7$ Hz , the observed RAO for roll is 9.5 and the predicted value is 12.5). It is also noted that predictions are larger for Configuration C than for Configuration A, a trend not confirmed by the experiments. This is probably not extremely relevant; however, since the real values of the observed rotations

in these conditions are small (for example, at f = 0.7 Hz, the scaling factor for the observed rotations is $H/(2*L) = 0.07/(2*3.0) = 0.012$ radians, i.e., 0.5 degrees).

5.2. Measured Wave Transmission

As for the RAOS, the experimental values of the transmission coefficient k_t are experimentally found for the subset of regular tests denoted in Figure 5 by a continuous line.

Figure 11 shows the experimental k_t for all configurations as a function of the frequency of the incident waves. The numerical predictions are also plotted in the same figure. The curve is very different from the typical S-shape trend. Both the data and the simulations confirm the presence of a stop band between 0.7 Hz and 1 Hz, approximately. For Configuration C, the lower experimental value is equal to 0.1, whereas for f < 0.7 Hz and f > 1.2 Hz, the observed transmission is larger than 80%.

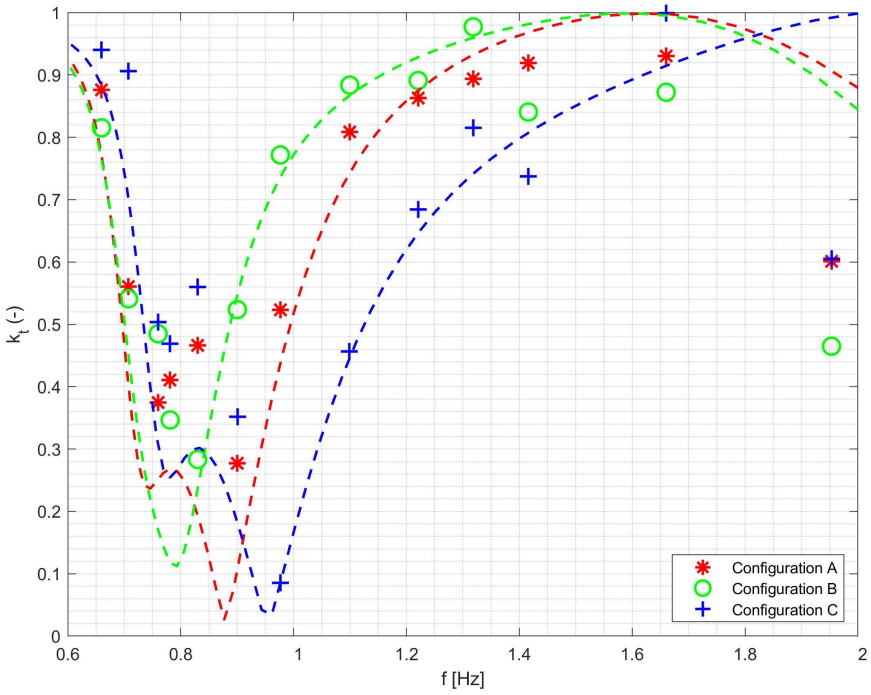

Figure 11. Experimental values of the k_t for the three tested configurations under regular waves. The numerical prediction is also shown.

The simple model used does not match the observed transmission coefficient quantitatively in all points (the maximum deviation occurs for Configuration C at f = 0.85 Hz, where the observed k_t value is 0.55 and the predicted one is 0.30). Nevertheless, the general trend of the curves matches the observations. In particular, (i) at high frequencies, the transmission decreases from Configuration B to A to C, and the experiments confirm this; (ii) the frequency of the lower k_t peak corresponds to the frequency of the observed lower k_t value (within a 0.05 Hz error); and (iii) the amplitude of the stop band frequency range is predicted with good accuracy (error lower than 0.05 Hz).

In order to extend the model to the irregular context, the spectrum of the transmitted irregular wave (for peak frequency ranging between 0.5 and 2 Hz) is computed by multiplying a JONSWAP incident wave spectrum by the square of the k_t curve computed numerically for regular waves. Figure 12 shows the obtained $k_{t(irr)}$ for all configurations under irregular waves. When the peak frequency of the considered irregular incident wave is large, the theoretical wave spectrum has considerable energy in the range of 2–5 Hz, i.e., outside the range of k_t shown in Figure 11. For simplicity, in this frequency range (2–5 Hz), the regular k_t is assumed equal to 0.5 for all configurations, and this also explains why all the predicted curves merge. After all, as anticipated the incident waves generated in the lab are a bit distorted for these high frequencies, which are filtered out to

avoid transversal waves. Hence, the data (and the predictions) may not be very accurate for high frequencies. Note that this extremely high-frequency range is not of interest for practical purposes.

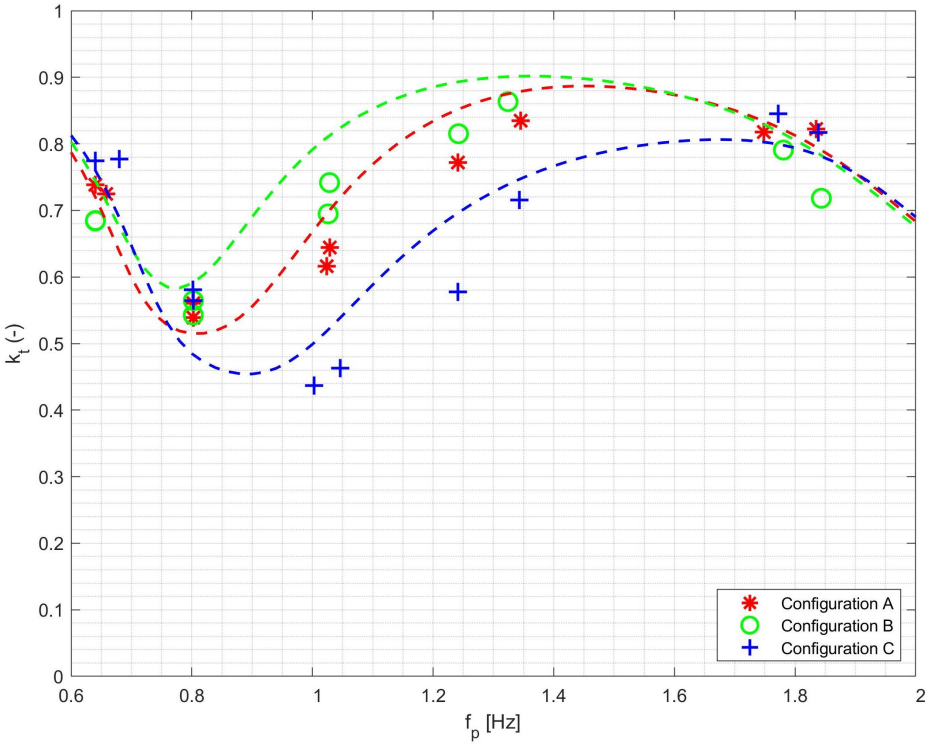

Figure 12. Experimental values of the k_t for the three tested configurations under irregular waves. The numerical prediction is also shown.

5.3. Sensitivity Analyses

In order to modify the position of the gravity center in a physically consistent way, the position of the gravity center is modified with a procedure that mimics what would actually happen in the laboratory should we vary the vertical position of the iron bars. The bars may be all placed in the center of the upper pipe (at depth $d_{Fe} = 0$), or all in the center of the lower pipe (at depth $d_{Fe} = 0.4$ like in the experiments) or split in order to obtain an intermediate depth of their gravity center. The numerical simulations take into account the position of the bars on the computation of the overall CG and the inertia.

Figure 13 shows the effect of the CG depth in terms of k_t. A lower gravity center is associated with a wider "filter", a lower transmission, and a shift in the peak to the higher frequencies. In particular, when the steel bars are at the free surface (at depth $d_{Fe} = 0$), the stop-band peak frequency is approximately 0.75 Hz, whereas when the steel bars are concentrated at the center of the lower pile (Configuration A where $d_{Fe} = 0.4$), the stop-band peak frequency is 9.2 Hz. The width of the stop-band frequency at $k_t = 0.5$ ranges approximately from 0 to 0.4 Hz, respectively, for the two mentioned cases.

The simulations are repeated starting from Configuration A, changing the distance d between the piles (see Figure 2). The mass and spring stiffness are unchanged, whereas the position of the gravity center, metacenter, and inertia are affected coherently. Consequently, the cases with d = 0.3 m and d = 0.4 m correspond respectively to Configurations A and C.

Figure 14 presents the results for different mutual distances between the vertical piles. A larger distance between the piles from 0.3 to 0.5 m is associated with a shift in the stop-band peak frequencies from 0.98 to 0.88 Hz. A further increase in the distance between the piles of 0.6 m does not affect the position of the stop-band peak, probably because the water depth is limited to 0.875 m, and therefore, the pipe is very close to the bed. The width of the stop-band is not significantly affected by this variable.

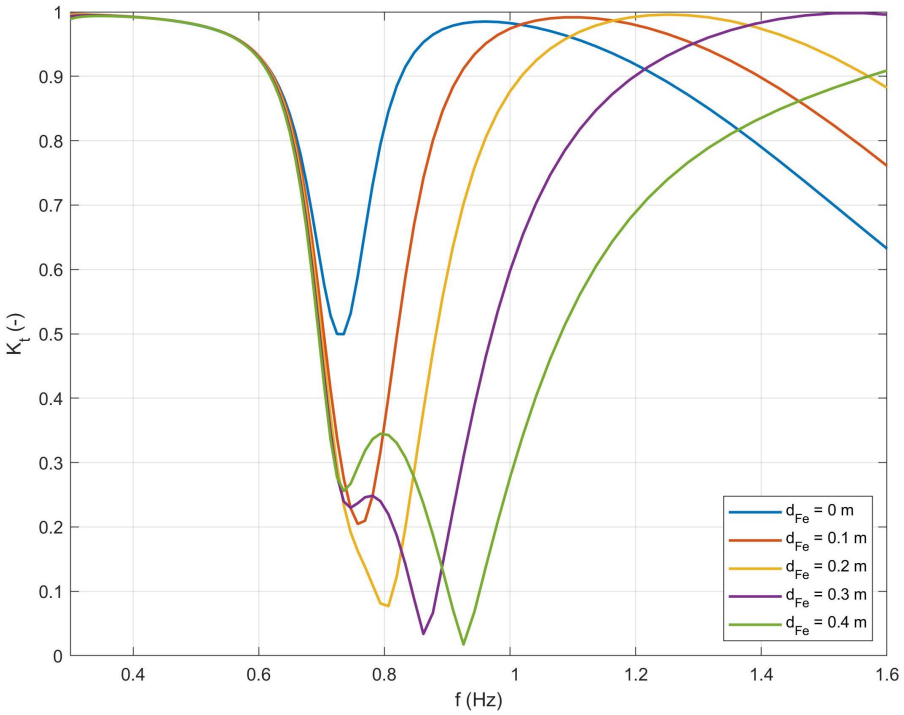

Figure 13. Experimental values of the k_t for different position of the ballast.

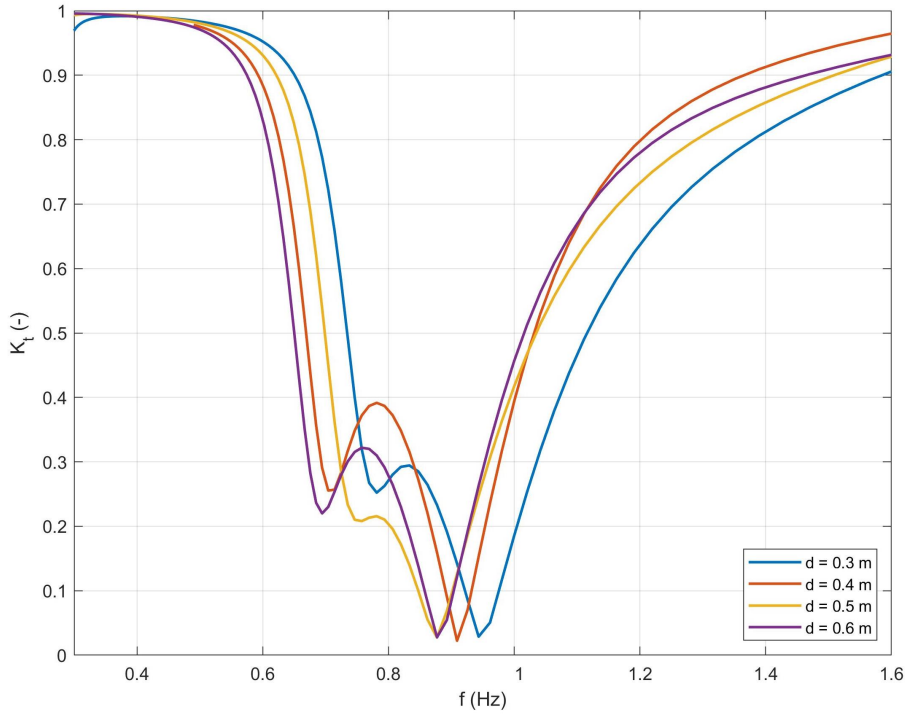

Figure 14. Experimental values of the k_t for different distances between the vertical piles.

Finally, the simulations are repeated starting from Configuration A and changing the global stiffness of the springs from 200 N/m to 3800 N/m in steps of 400 N/m.

Figure 15 presents the results. It may be observed that a larger stiffness is associated with a wider stop-band filter and a shift in the peak to the higher frequencies. It is, in fact, expected that for a stiffer system, the eigenfrequency increases.

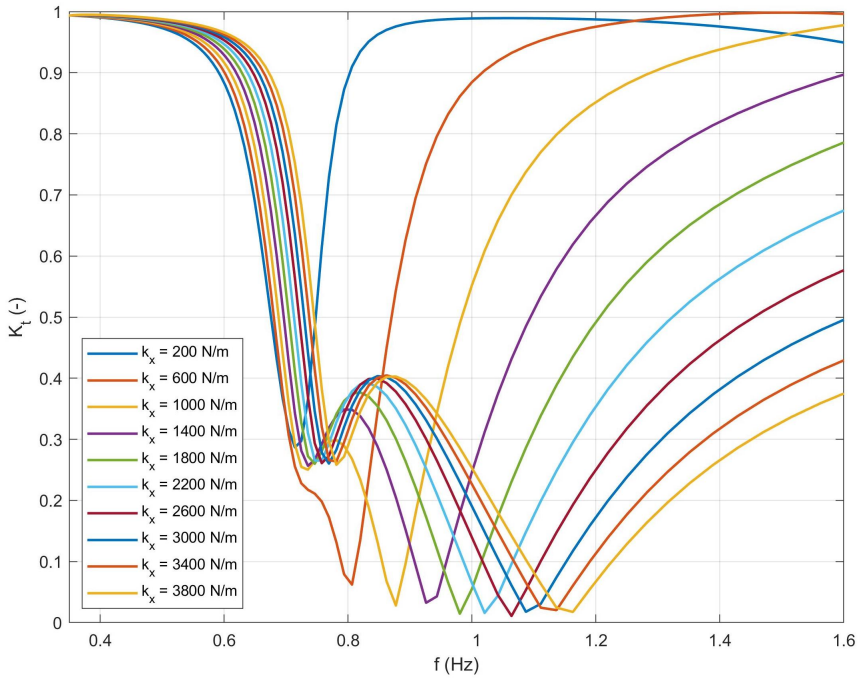

Figure 15. Experimental values of the k_t for different values of the global stiffness.

6. Conclusions

This paper investigated experimentally and numerically the behavior of a novel floating breakwater. The FB is comprised of two or three vertically aligned and rigidly connected PVC pipes moored with sub-horizontal elastic lines.

The incident, reflected, and transmitted waves are observed through two sets of four resistive wave gauges, and the wave transmission coefficient is given for a set of regular waves. The dynamic motions are captured by a two-megapixel webcam situated in frontal alignment with the wave flume glass. The experimental Response Amplitude Operators are given for heave, sway, and roll oscillation.

The presence of a stop-band is clearly visible but less pronounced for the tests under irregular waves.

The measured k_t is not a typical S-shaped curve but rather a stop-band. A simple numerical investigation is set up, based on a simple linear potential flow model, that confirms such behavior.

By a sensitivity analysis carried out with the linear model, it is observed that lowering the gravity center increases the stop-band effect. The width of the stop-band also increases with the stiffness of the structure and the radius of gyration (distance between the pipes).

It should be noted that all experimental and numerical data in this work are for multi-cylindrical FBs in model scale. Thus, with regard to full-scale investigations, there are unknown scale effects. In the numerical model, the drag is included as an added vertical damping term. The viscous damping is typically larger in model scale than in full scale. As the damping term at model scale is in the same order as the hydrodynamic damping, scale effects should be properly investigated before full-scale designs are developed based on the present study. Further investigations require the setup of more accurate numerical models, simulating (in a non-linear context) also the tests carried out with larger regular waves and under irregular wave conditions (e.g., CFD to investigate possible turbulent energy dissipation occurring in the gaps between cylinders, similarly, for instance, to the study carried out in [22]).

Author Contributions: Conceptualization, M.A.; methodology, L.M.; software, L.M., M.V. and O.M.; formal analysis, L.M.; experimental investigation, M.V. and L.M.; writing—original draft preparation, L.M.; writing—review and editing, O.M. and C.E. All authors have read and agreed to the published version of the manuscript.

Funding: This research was partly funded by PNRR MUR—M4C2—Investimento 1.3—Extended Partnership—"NEST"—Intervention area "2—Future energy scenarios" (Id. Code PE00000021)—Spoke 5 "Energy conversion" CUP C93C22005230007. The support of Centro Levi Cases and Sizable Energy S.r.l. is also acknowledged.

Data Availability Statement: The data presented in this study are available in the permanent repository "Padua Research Archive", https://researchdata.cab.unipd.it (accessed on 22 August 2024), reference number 1345.

Conflicts of Interest: Author Manuele Aufiero is the CEO of the company Sizable Energy S.r.l. The funding sponsors designed the prototype structure and gave their consent to publish the results, but had no role in the collection, analyses, or interpretation of the data.

Abbreviations

The following abbreviations are used in this manuscript:

CG	Center of Gravity
DoF	Degree of Freedom
FB	Floating Breakwater
HDPE	Extruded High-Density Polyethylene
RAO	Response Amplitude Operator

Appendix A. Numerical Model

The model solves the equation of motion of the FB when the FB is free to oscillate along the horizontal and vertical direction (sway and heave, respectively) and rotate around the longitudinal direction (roll).

The fluid motion can be described in terms of the velocity potential ϕ, satisfying the Laplace equation:

$$\nabla^2 \phi = 0 \tag{A1}$$

As the problem is linear, the potential can be conveniently written as a superposition of incident (ϕ_I), diffracted (ϕ_D), and radiated potentials (ϕ_R):

$$\phi = \phi_I + \phi_D + \sum_j \phi_{R_j} v_j \tag{A2}$$

where the radiated potential, in turn, is decomposed in a sum of "unit radiated potentials" ϕ_{R_j} (i.e., the radiated potential evaluated for unit velocity) multiplied by their respective rigid body velocity component v_j, and the index j denotes the three modes of oscillations (sway, heave, and pitch). In a context where the selected incident potential satisfies the Laplace equation, the application of Equation (A1) requires that the diffraction and the unit radiation potentials must also conform to the Laplace equation.

Today's standard numerical procedure is to solve the potential on the boundary of the floating body, applying Green's theorem through the Boundary Element Method (BEM); see [36]. It has been recognized that the application of the BEM is beneficial since the unknowns are only computed in the panels needed to discretize the floating body hull, rather than in all the mesh elements that describe the body of water in contact with the floating body. The method obviously requires a suitable Green function, and this may introduce some complications in the case of complex bathymetries.

The model used in this paper instead solves the Laplace equation (Equation (A1)) using the finite element method (FEM) [37,38] to find the diffraction and unit radiation potentials. In the analyzed case, the problem is essentially two dimensional, which greatly reduces the computational effort. The computational domain is $x \in [-10, 10]$ m in order to include waves with a frequency up to 1.4 Hz. The computational mesh is made up of triangles with a total of $N = 2437$ nodes, see Figure A1. The numerical solution requires assembling and inverting a matrix with a size that is N^2.

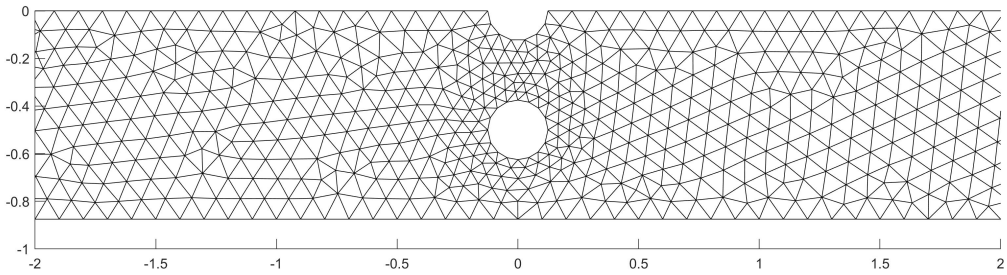

Figure A1. Example of mesh of the domain around the cylinders.

The boundary value problem is solved for the different configurations and wave periods ranging from 0.6s to 4.0s, with a wave height of unity, providing the potentials ϕ_D and ϕ_{R_j}. Figure A2 shows an example of the real part of the diffraction potential for an incident wave of $T = 0.9$s entering the domain from the left.

Figure A2. Real part of the diffracted potential for an incident wave ($T = 0.9$s) entering the domain from the left.

The hydrodynamic force is computed from the diffracted potential and the added mass, and the damping coefficients are computed based on the unit radiated potentials. More specifically, the Froude–Krylov and the diffraction force are obtained by integrating over the rigid body the pressure that is proportional to the incident and diffracted potentials:

$$F_{W_j} = F_{I_j} + F_{D_j} = i\rho\omega \int_S (\phi_I + \phi_D) n_j \, dS \tag{A3}$$

where F_I, F_D, and F_W are respectively the incident, the Froude–Krylov, the diffraction, and the exciting wave forces, and the index j denotes the direction of the translation oscillations modes (1 = horizontal, 2 = vertical). The force moment (with index 3 for rotational mode) is obtained by

$$F_{W3} = F_{I3} + F_{D3} = i\rho\omega \int_S (\phi_I + \phi_D)(\vec{s} \times \vec{n}) \, dS \tag{A4}$$

The unit radiation force is found as the integral of the pressures of the unit radiated potentials ϕ_R (computed assuming unit body velocity), and the added mass matrix A and the damping coefficient matrix B are defined (for the translation modes 1 and 2) by

$$A_{jk} + \frac{iB_{jk}}{\omega} = \rho \int_S \phi_{Rk} n_j \, dS \tag{A5}$$

where $j = 1, 2$ and $k = 1, 2, 3$. Since the vertical motion is independent of the others (i.e., it does not produce horizontal forces nor moment of the force), $A_{21} = A_{12} = A_{23} = A_{32} = 0$ and $B_{21} = B_{12} = B_{23} = B_{32} = 0$. The similar expressions relative to the rotational modes are

$$A_{3k} + \frac{iB_{3k}}{\omega} = \rho \int_S \phi_{Rk} (\vec{s} \times \vec{n}) \, dS \tag{A6}$$

and the two matrices are symmetric and positive.

According to Newton's second law, the floating body dynamic movements can be found by

$$[M]\{\ddot{\vec{x}}\} + [K]\{\vec{x}\} = [F_W] - [A]\{\ddot{\vec{x}}\} - [B]\{\dot{\vec{x}}\} \tag{A7}$$

where M_{jk} is the mass matrix, K_{jk} is the stiffness and includes both the hydro-static restoring force and the effects of the mooring springs, F_{Wj} is the exciting wave force or moment, and x_j describes the rigid body oscillations.

In the frequency domain, the periodic contribution can be separated with $e^{-i\omega t}$ such as

$$\begin{cases} \vec{x} = \vec{\xi} e^{-i\omega t} \\ \vec{F_w} = \vec{f_W} e^{-i\omega t} \end{cases} \tag{A8}$$

where t represents the time, and $\vec{\xi}$ and $\vec{f_w}$ respectively represent the amplitude of the responses of the motion and the wave exciting forces. Substituting Equation (A8) into Equation (A7) yields the following:

$$(-\omega^2[M+A] \ - i\omega[B]+[K])\{\xi\} = \{f_w\} \tag{A9}$$

The body velocity is given by

$$\vec{v} = \frac{d\vec{x}}{dt} = i\omega\xi e^{-i\omega t} \tag{A10}$$

As shown in Equation (A2), the actual radiation potential is determined by the product of the unit radiation potential (i.e., the radiated potential evaluated for unit velocity) and the actual rigid body velocity, which is now obtained by Equations (A9) and (A10).

In conclusion, after the diffracted and the unit radiated potentials ϕ_D and ϕ_{Rj} are found by the LPF model, the RAOs and the k_t can be found through the following steps:

(i) Find the wave exciting forces f_w through Equations (A3), (A4) and (A8)—an example of f_w for the translation modes is shown in Figure A3, upper panel (in the figure, $\rho\Delta$ is the overall mass).
(ii) Obtain the added mass A and damping coefficients B determined by unit radiation wave pote ntial (i.e., assuming unit body velocity) through Equation (A5) (an example if the translation modes is shown in Figure A3, lower panel).
(iii) Find the frequency domain responses using Equation (A9) and hence the RAOs.
(iv) Compute the body velocity by Equation (A10).
(v) Build the actual velocity potential as the sum of the incident, diffracted, and radiated potentials (the unit radiation multiplied by the computed body velocity) as shown in Equation (3).
(vi) Extract from the actual velocity potential the transmitted and incident wave height, and hence k_t.

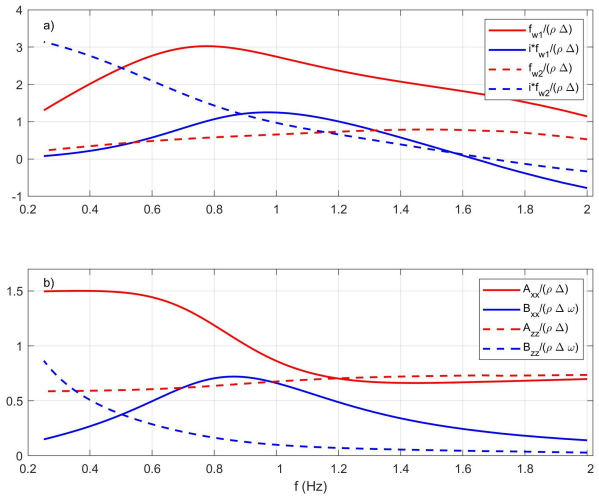

Figure A3. Results for Configuration A, translation modes: (**a**) Non-dimensional exciting wave force. (**b**) Non-dimensional added mass and damping coefficient.

References

1. Smith, K.N. After D-Day, These Floating Harbors Helped Win WWII. *Forbes*, 6 June 2021. Available online: https://www.forbes.com/sites/kionasmith/2021/06/06/after-d-day-these-floating-harbors-helped-win-wwii (accessed on 20 June 2023).
2. Katoh, J. Assessment of floating breakwaters. In *Marine Behaviour and Physiology*; Taylor & Francis _Eprint: Abingdon, UK , 1992; Volume 20, pp. 1–212. [CrossRef]
3. Dai, J.; Wang, C.M.; Utsunomiya, T.; Duan, W. Review of recent research and developments on floating breakwaters. *Ocean Eng.* **2018**, *158*, 132–151. [CrossRef]
4. McCartney, B.L. Floating breakwater design. *J. Waterw. Port Coast. Ocean Eng.* **1985**, *111*, 304–318. [CrossRef]
5. Oliver, J.; Aristaghes, P.; Cederwall, K.; Davidson, D.; De Graaf, F.; Thackery, M.; Torum, A. Floating Breakwaters: A Practical Guide for Design and Construction. Available online: https://www.pianc.org/publication/floating-breakwaters-a-practical-guide-for-design-and-construction/ (accessed on 31 August 2024).
6. Macagno, E. Fluid mechanics—Experimental study of the effects of the passage of a wave beneath an obstacle. In Proceedings of the Academic des Sciences, Paris, France, 19–24 June 1953.
7. Brebner, A.; Ofuya, A.O. Floating Breakwaters. *Coast. Eng. Proc.* **1968**, *1*, 68. [CrossRef]
8. Hom-ma, M.; Horikawa, K.; Mochizuki, H. An experimental study on floating breakwaters. *Coast. Eng. Jpn.* **1964**, *7*, 85–94. [CrossRef]
9. Katō, J.; Hagino, S.; Uekita, Y. Damping effect of floating breakwater to which anti-rolling system is applied. In *Coastal Engineering 1966*; ASCE: Reston, VA, USA , 1967; pp. 1068–1078.
10. Ruol, P.; Martinelli, L.; Pezzutto, P. Formula to predict transmission for π-type floating breakwaters. *J. Waterw. Port Coast. Ocean Eng.* **2013**, *139*, 1–8. [CrossRef]
11. Ji, C.Y.; Chen, X.; Cui, J.; Gaidai, O.; Incecik, A. Experimental study on configuration optimization of floating breakwaters. *Ocean Eng.* **2016**, *117*, 302–310. [CrossRef]
12. Dobnigg, A. Three 350-m-Long, Large Diameter HDPE Pipes Travel the Atlantic to be Sunk in the Caribbean. Available online: https://www.pipelife.com/content/wps/wpsint/main-website/en/service/news-and-projects/large-diameter-hdpe-pipes-travel-the-atlantic-to-be-sunk-in-the-caribbean.html/ (accessed on 31 August 2024).
13. Ursell, F. On the heaving motion of a circular cylinder on the surface of a fluid. *Q. J. Mech. Appl. Math.* **1949**, *2*, 218–231. [CrossRef]
14. Dean, R.G.; Ursell, F. *Interaction of a Fixed, Semi-Immersed Circular Cylinder with a Train of Surface Waves*; Massachusetts Institute of Technology, Hydrodynamics Laboratory: Cambridge, MA, USA, 1959.
15. Yu, Y.; Ursell, F. Surface waves generated by an oscillating circular cylinder on water of finite depth: Theory and experiment. *J. Fluid Mech.* **1961**, *11*, 529–551. [CrossRef]
16. Borgman, L. Computation of the Ocean Forces on an Infinitely Long Circular Cylinder in an Oblique Sea. *Trans. Am. Geophys. Union* **1958**, *39*, 885–888.
17. Frank, W. *Oscillation of Cylinders in or below the Free Surface of Deep Fluids*; Naval Ship Research and Development Center: Washington DC, USA, 1967; Volume 2375.
18. Yeung, R.W. Added mass and damping of a vertical cylinder in finite-depth waters. *Appl. Ocean Res.* **1981**, *3*, 119–133. [CrossRef]
19. Martin, P.A.; Dixon, A.G. The scattering of regular surface waves by a fixed, half-immersed, circular cylinder. *Appl. Ocean Res.* **1983**, *5*, 13–23. [CrossRef]
20. Wang, S.; Wahab, R. Heaving oscillations of twin cylinders in a free surface. *J. Ship Res.* **1971**, *1*, 33–48.
21. Bihs, H.; Ong, M.C. Numerical simulation of flows past partially-submerged horizontal circular cylinders in free surface waves. In Proceedings of the International Conference on Offshore Mechanics and Arctic Engineering, Nantes, France, 9–14 June 2013; American Society of Mechanical Engineers: New York, NY, USA, 2013; Volume 55416, p. V007T08A036.
22. Ong, M.C.; Kamath, A.; Bihs, H.; Afzal, M.S. Numerical simulation of free-surface waves past two semi-submerged horizontal circular cylinders in tandem. *Mar. Struct.* **2017**, *52*, 1–14. [CrossRef]
23. Cheng, X.; Liu, C.; Zhang, Q.; He, M.; Gao, X. Numerical Study on the Hydrodynamic Characteristics of a Double-Row Floating Breakwater Composed of a Pontoon and an Airbag. *J. Mar. Sci. Eng.* **2021**, *9*, 983. [CrossRef]
24. Deng, X.; Liu, S.; Ong, M.C.; Ji, C. Numerical simulations of free-surface waves past two vertically aligned horizontal circular cylinders. *Ocean Eng.* **2019**, *172*, 550–561. [CrossRef]
25. Dixon, A.G.; Salter, S.H.; Greated, C.A. Wave Forces on Partially Submerged Cylinders. *J. Waterw. Port Coast. Ocean Div.* **1979**, *105*, 421–438. [CrossRef]
26. Ozeren, Y.; Wren, D.G.; Altinakar, M.; Work, P.A. Experimental Investigation of Cylindrical Floating Breakwater Performance with Various Mooring Configurations. *J. Waterw. Port Coast. Ocean Eng.* **2011**, *137*, 300–309. [CrossRef]
27. Akgul, M. Effect of Pipe Spacing on the Performance of a Trimaran Floating Pipe Breakwater. In Proceedings of the ISOPE 2016, Rhodes, Greece, 26 June–1 July 2016.
28. Kagemoto, H.; Yue, D.K. Interactions among multiple three-dimensional bodies in water waves: An exact algebraic method. *J. Fluid Mech.* **1986**, *166*, 189–209. [CrossRef]
29. Abul-Azm, A.G.; Gesraha, M.R. Approximation to the hydrodynamics of floating pontoons under oblique waves. *Ocean Eng.* **2000**, *27*, 365–384. [CrossRef]
30. Gesraha, M.R. Analysis of Π shaped floating breakwater in oblique waves: I. Impervious rigid wave boards. *Appl. Ocean Res.* **2006**, *28*, 327–338. [CrossRef]

31. Martinelli, L.; Ruol, P.; Zanuttigh, B. Wave basin experiments on floating breakwaters with different layouts. *Appl. Ocean Res.* **2008**, *30*, 199–207. [CrossRef]
32. Zelt, J.; Skjelbreia, J.E.; Wave, T. Estimating incident and reflected wave fields using an arbitrary number of wave gages. In Proceedings of the International Conference on Computers in Education (ICCE), Singapore, 7–10 December 1992; World Scientific Pub Co Inc.: Singapore, 1993, Volume 1, pp. 777–788.
33. Falnes, J. *Ocean Waves and Oscillating Systems: Linear Interactions Including Wave-Energy Extraction*; Cambridge University Press: Cambridge, UK, 2002. [CrossRef]
34. Kramer, M.B.; Andersen, J.; Thomas, S.; Bendixen, F.B.; Bingham, H.; Read, R.; Holk, N.; Ransley, E.; Brown, S.; Yu, Y.H.; et al. Highly Accurate Experimental Heave Decay Tests with a Floating Sphere: A Public Benchmark Dataset for Model Validation of Fluid–Structure Interaction. *Energies* **2021**, *14*, 269. [CrossRef]
35. MathWorks Inc. *Image Processing Toolbox Reference*; MathWorks Inc.: Natick, MA, USA, 2024. Available online: www.mathworks.com (accessed on 15 June 2024).
36. Brebbia, C.A.; Walker, S. *Boundary Element Techniques in Engineering*; Elsevier: Amsterdam, The Netherlands, 2016.
37. Sjökvist, L.; Göteman, M.; Rahm, M.; Waters, R.; Svensson, O.; Strömstedt, E.; Leijon, M. Calculating buoy response for a wave energy converter—A comparison of two computational methods and experimental results. *Theor. Appl. Mech. Lett.* **2017**, *7*, 164–168. [CrossRef]
38. Visbech, J.; Engsig-Karup, A.P.; Bingham, H.B. Solving the complete pseudo-impulsive radiation and diffraction problem using a spectral element method. *Comput. Methods Appl. Mech. Eng.* **2024**, *423*, 116871. [CrossRef]